

High-Frequency Electric Machines for Boundary Layer Ingestion Fan Propulsor

Andy Yoon , Jianqiao Xiao , Danny Lohan, Faraz Arastu, and Kiruba Haran , *Fellow, IEEE*

Abstract—High specific power electric motor is a key enabling technology for electric/hybrid-electric propulsion for aircraft. High-frequency, air core machine topologies show potential for high specific power when the machines are integrated within jet engines at high speed, e.g. 15,000 rpm. In this paper, we explore how these machines scale to a boundary layer ingestion (BLI) fan application in newly proposed Single-aisle Turboelectric Aircraft with an Aft Boundary Layer Propulsor (STARC-ABL). Detailed analytical models that have been experimentally verified, and an evolutionary genetic algorithm are utilized to choose an optimized design for the BLI propulsor. Analyses show that a 2.6 MW, 11 kW/kg, 98% electric motor is achievable.

Index Terms—Electrical machines, high specific power, high power density, high-frequency, electric propulsion, electric aircraft, slotless, STARC-ABL.

I. INTRODUCTION

NATIONAL Aeronautics and Space Administration (NASA) has identified light-weight electric motors as a key enabling technology to reduce thrust specific fuel and energy consumption of aircrafts [1], [2]. Such motors achieve high specific power through aggressive cooling and high speed [3]–[5]. One example of a high-frequency machine with a significantly reduced ferromagnetic core is a 13 kW/kg, 1 MW machine being developed by NASA [6]. The design of the machine is optimized at 15,000 rpm to be integrated within a jet engine in a parallel-hybrid or turbo-electric propulsion systems. However, most aircraft designs use lower rotational speeds for propulsors. This paper builds on work from earlier paper by the authors, which shows that a motor with high fundamental frequency and a slotless topology retains high specific power characteristics at lower rotational speeds [7].

Specific target application of this paper is the tail-cone propulsor for the NASA's newly proposed turboelectric concept aircraft, STARC-ABL, which is shown in Fig. 1. The 2.6 MW,



Fig. 1. STARC-ABL concept with BLI fan indicated.

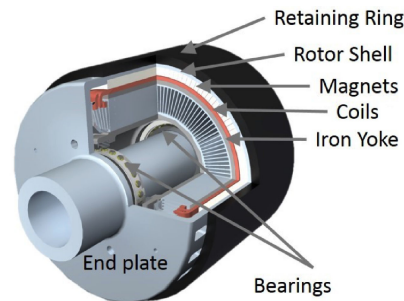


Fig. 2. CAD representation of the full motor.

3000 rpm boundary layer propulsor allows reduction of drag that exists on the fuselage of an aircraft by “ingesting” the hydrodynamic boundary layer that exists on the surface, which allows for a significant reductions in system fuel burn [8], [9]. This paper first presents a brief overview of the baseline design of the motor, followed by analytical models used for sizing the boundary layer ingestion (BLI) fan motor. Several possibilities for motor-propulsor integration is presented and compared, and a final design is chosen based on pareto line comparing weight and efficiency.

II. BASELINE MOTOR CONCEPT SUMMARY

In Fig. 2, the concept of the motor is highlighted. High specific power is achieved through the use of high-frequency to minimize the magnetic circuit of the motor, reducing the amount of heavy metal in the design. For motors with high fundamental frequency, we can assume that the thicknesses of the stator yoke, d_s , and rotor yoke, d_r , are much smaller than the airgap diameter. Then, expressing power density as power (from the well-known sizing equation) divided by volume of active materials, we see

Manuscript received April 8, 2019; revised August 14, 2019; accepted September 2, 2019. Date of publication September 19, 2019; date of current version November 21, 2019. This work was supported by NASA under a Small Business Innovation Research (SBIR) Program Award Contract 80NSSC18P1898. Paper no. TEC-00409-2019. (*Corresponding author: Andy Yoon.*)

A. Yoon, J. Xiao, and K. Haran are with the Department of Electrical and Computer Engineering, University of Illinois at Urbana-Champaign, Urbana, IL 61801 USA (e-mail: yoon62@illinois.edu; jxiao14@illinois.edu; kharan@illinois.edu).

D. Lohan and F. Arastu are with the Hinetics, LLC, Champaign, IL 61820 USA (e-mail: dlohan@hinetics.com; farastu@hinetics.com).

Color versions of one or more of the figures in this article are available online at <http://ieeexplore.ieee.org>.

Digital Object Identifier 10.1109/TEC.2019.2942775

that

$$\text{Power Density} \approx \frac{2k_w A_{peak} B_{peak} v}{d_s + d_r}, \quad (1)$$

where k_w , A , B , and v refer to winding factor, electrical loading, magnetic loading, and rotor tipspeed. The expression points to the usual emphasis on cooling and adoption of better magnetic materials to maximize electrical loading and magnetic loading, respectively, to maximize power density. Density of active materials such as steel, copper (especially including insulation), and magnets are of same order, so the above expression can be said to be proportional to specific power. Note that for a more accurate representation of specific power, auxiliary components such as structural and cooling infrastructure must be taken into account. The expression also highlights that high-frequency machines can achieve high specific power through high rotor tipspeed, regardless of size or angular speed. This is especially attractive in aircraft propulsion systems because typical aircraft fans rotate around 3000 rpm. To accommodate high-frequency and high rotor tip speed, appropriate design choices have been made. Adoption of litz wires (for high-frequency armature coils) and elimination of stator teeth alleviate the electrical and magnetic losses associated with high-frequency. Energy-dense, rare-earth permanent magnets in the rotor are arranged in a Halbach array, eliminating the need for a rotor yoke. An outer carbon fiber ring is used to retain the magnets at high tip speeds. The use of outer-rotor topology allows proper thickness of retaining ring without sacrificing the magnetic air-gap between the magnet and the high-frequency coils.

The resulting air-core topology allows more space and flexibility in the design of a heat sink along the inner diameter of the stator. Along with a ducted fan design that pulls the air in from the free-end of the cantilevered design, the heat sink allows for effective extraction of thermal losses from the high-frequency coils. The armature consists of a 3-phase, 20-pole distributed winding with 2 slots per pole per phase (10 pre-cast coils per phase), and a 5/6th winding pitch. Armature coils are precast using ceramic filled resin to further improve thermal performance from the copper. To improve manufacturing and assembly qualities of the coils, coils of each phase are staggered with respect to coils of another phase. The resulting coils have different end-winding length between the phases, but can easily be addressed with appropriate drive control. Design and prototyping effort of this 1 MW motor included development effort of a modular, multilevel inverters that have shown to be effective at minimizing total harmonic distortion (THD) [10]. This, coupled with a highly sinusoidal airgap field, also allows the topology to have very low torque ripple. Key metrics of the baseline motor being developed are summarized in Table I. The 1 MW prototype motor hardware is shown in Fig. 3.

III. ANALYTICAL MODEL

An analytical model for the air-core machine described in the previous section has been developed to predict electromagnetic, thermal, and mechanical performance, as described in the following subsections. The loss models have been validated and calibrated with recent experiments [11], [12] and serve as

TABLE I
KEY METRICS AND DIMENSIONS FOR THE BASELINE MOTOR

Rated Power	1	MW
Rated Efficiency	96	%
Nominal Speed	15,000	rpm
Cooling, Forced air	20	m/s
Tip Speed	270.3	m/s
Outer Diameter	13.55	in.
Number of Poles	20	-
Phases	3	-
PM Radial Thickness	0.49	in.
Air-gap Diameter	11.25	in.
Coil Radial Thickness	0.23	in.
Stator Yoke Radial Thickness	0.31	in.
Stack Length	9.5	in.
Specific Power	13	kW/kg
Total Weight	77	kg

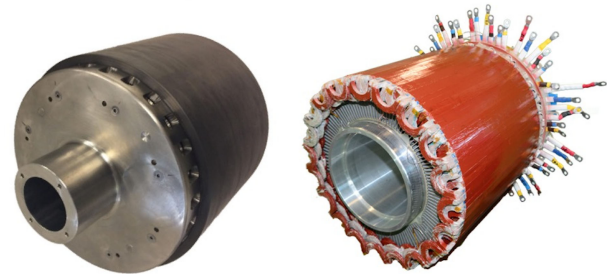


Fig. 3. Rotor (left) and stator (right) assembly of the 1 MW motor.

the starting point for obtaining an optimal design for the BLI propulsor motor. As one of the main fixed variable constraint for the optimization is air-gap heat flux, the losses are represented in the form of heat flux. Furthermore, only copper losses, iron losses, and windage losses are considered for this study. Study of the 1 MW baseline design showed that magnet losses and bearing losses are very small compared to the other losses (0.5% for magnet loss and 0.2% for bearing) and thus are excluded from the analysis [13].

A. Air-Gap Field and Torque

While finite element method (FEM) provides highly accurate field distribution in the air-gap, it is not suitable for comparative studies with dozens of cases due to its high computation time. In the case of conventional machines characterized by small air-gap distance, magnetic equivalent circuit (MEC) model is often used. In the case of a toothless, air-gap winding topology, simplified model such as MEC should be avoided because of the larger magnetic air-gap and the resulting increase in air-gap leakage. Thus, to calculate air-gap field for a given geometry and the resulting torque, an analytical model (shown in Fig. 4) based on flux-potential transfer relations is used [14].

We begin with the fact that

$$\mathbf{B}_n = \mu_o (\mathbf{H}_n + \mathbf{M}_n), \quad (2)$$

where \mathbf{M} is magnetization intensity vector. Applying curl on both sides,

$$\nabla \times \mathbf{B}_n = \mu_o \nabla \times \mathbf{M}_n \quad (3)$$

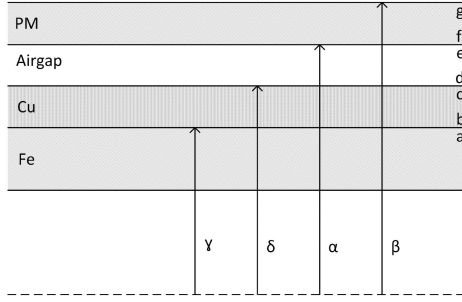
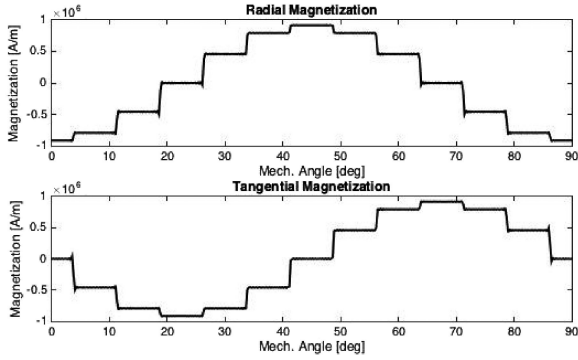


Fig. 4. Analytical model for the toothless topology.


 Fig. 5. Radial magnetization, M_r , and tangential magnetization, M_θ , for one pole pair of an 8-pole design. The results here show sum of up to 100th harmonic contents.

can be established with the fact that the permanent magnet region is absent of free current such that the Ampere's law gives $\nabla \times \mathbf{H}_n = 0$. Expressing \mathbf{B}_n in terms of magnetic vector potential,

$$\begin{aligned} \nabla \times \mathbf{B}_n &= \nabla \times (\nabla \times \mathbf{A}_n) \\ &= \nabla (\nabla \cdot \mathbf{A}_n) - \nabla^2 \mathbf{A}_n \end{aligned} \quad (4)$$

Finally, using the Coulomb gauge condition, (3) and (4) can be combined to establish a Poisson's equation as shown as,

$$\nabla^2 \mathbf{A}_n = -\mu_o \nabla \times \mathbf{M}_n, \quad (5)$$

where the subscript n denotes the harmonic number to account for non-sinusoidal magnetization vector. Assuming a general form of \mathbf{A}_n and \mathbf{M}_n such that

$$\begin{aligned} \mathbf{A}_n &= \text{Re} [A_{z,n} e^{-jn p \theta}] \hat{\mathbf{z}} \\ \mathbf{M}_n &= [M_{r,n} e^{-jn p \theta} \hat{\mathbf{r}} + M_{\theta,n} e^{-jn p \theta} \hat{\boldsymbol{\theta}}], \end{aligned} \quad (6)$$

(5) can be solved as

$$\frac{\partial^2}{\partial r^2} A_{z,n} + \frac{1}{r} \frac{\partial}{\partial r} A_{z,n} - \left(\frac{np}{r}\right)^2 A_{z,n} = -j\mu_o \frac{np}{r} M_n, \quad (7)$$

where r , p and θ refer to radius, number of pole pairs, and angular position, respectively. $A_{z,n}$, $M_{r,n}$, and $M_{\theta,n}$ refer to magnitudes of magnetic vector potential, radial magnetization vector, and tangential magnetization vector, of n^{th} harmonic. Variable M_n is calculated as $M_{r,n} + M_{\theta,n}/jnp$. Fig. 5 shows an example of

radial and tangential magnetization magnitudes for an Halbach array.

Upon finding homogeneous and particular solution for (7), general transfer relation between the magnetic vector potentials and the tangential flux densities at two different boundaries can be established. For example, from Fig. 4, tangential flux density at boundary, f (with radius of α), and tangential flux density at boundary, g (with radius of β), can be described with the following transfer relation:

$$\begin{bmatrix} B_{\theta n}^f \\ B_{\theta n}^g \end{bmatrix} = \begin{bmatrix} F_o(\beta, \alpha) & G_o(\alpha, \beta) \\ G_o(\beta, \alpha) & F_o(\alpha, \beta) \end{bmatrix} \begin{bmatrix} A_{z,n}^f \\ A_{z,n}^g \end{bmatrix} - M_s \begin{bmatrix} X_s \\ Y_s \end{bmatrix}, \quad (8)$$

where

$$\begin{aligned} M_s &= \frac{j\mu_o np M_n}{(np)^2 - 1}, \\ X_s &= \alpha F_o(\beta, \alpha) + \beta G_o(\alpha, \beta) + 1, \\ Y_s &= \alpha G_o(\beta, \alpha) + \beta F_o(\alpha, \beta) + 1, \end{aligned}$$

and functions, F_0 and G_0 , can be calculated as

$$\begin{aligned} F_0(x, y) &= \frac{np}{y} \frac{\left[\left(\frac{x}{y}\right)^{np} + \left(\frac{y}{x}\right)^{np}\right]}{\left[\left(\frac{x}{y}\right)^{np} - \left(\frac{y}{x}\right)^{np}\right]}, \\ G_0(x, y) &= \frac{2np}{x} \frac{1}{\left[\left(\frac{x}{y}\right)^{np} - \left(\frac{y}{x}\right)^{np}\right]} \end{aligned}$$

Applying boundary condition of $H_\theta^e = H_\theta^f$ and (3) results in a transfer relation between boundaries e and h as

$$\begin{bmatrix} B_{\theta n}^e \\ B_{\theta n}^h \end{bmatrix} = \begin{bmatrix} F_o(\beta, \alpha) & G_o(\alpha, \beta) \\ G_o(\beta, \alpha) & F_o(\alpha, \beta) \end{bmatrix} \begin{bmatrix} A_{z,n}^e \\ A_{z,n}^h \end{bmatrix} + \begin{bmatrix} -\mu_o M_{\theta,n} - M_s X_s \\ -\mu_o M_{\theta,n} - M_s Y_s \end{bmatrix}. \quad (9)$$

Furthermore, noting that magnetization source does not exist between boundaries b and e , the transfer relation can be shown as

$$\begin{bmatrix} B_{\theta n}^b \\ B_{\theta n}^e \end{bmatrix} = \begin{bmatrix} F_o(\alpha, \gamma) & G_o(\gamma, \alpha) \\ G_o(\alpha, \gamma) & F_o(\gamma, \alpha) \end{bmatrix} \begin{bmatrix} A_{z,n}^b \\ A_{z,n}^e \end{bmatrix}. \quad (10)$$

Then, combining (8), (9), and (10), with a boundary condition stating that $B_\theta^b = 0$, we can obtain B_θ^e and B_θ^h . From these results, tangential flux densities at all boundaries can be computed using the transfer relations. Radial component of the flux density can simply be obtained by computing the curl of magnetic vector potential. Fig. 6 shows the flux density of the Halbach array using the described transfer relations. Note that the non-active side result shows the effectiveness of field cancellation.

Similarly, Poisson's equation can be obtained for finding magnetic field due to the coils, as shown as

$$\nabla^2 \mathbf{A}_n = -\mu_o \nabla \times \mathbf{J}_f. \quad (11)$$

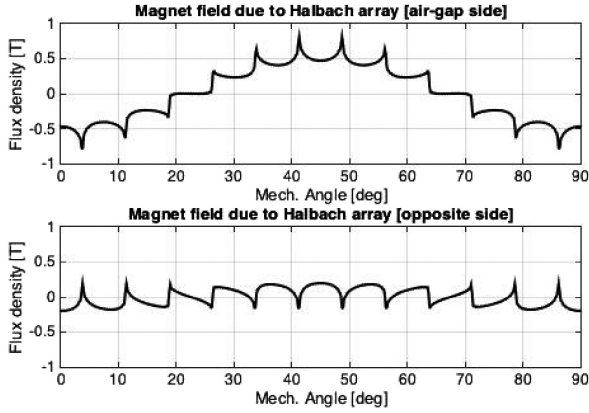


Fig. 6. Magnet flux density at Halbach array magnet surface. Air-gap side (top), and non-active side (bottom).

where \mathbf{J}_f refers to current density of the coils. Then the transfer relation between the magnetic vector potentials and the tangential flux densities at two different boundaries (e.g. boundaries denoted by b (with radius of γ) and c (with radius of δ)) due to the coils can be shown as

$$\begin{bmatrix} B_{\theta n}^b \\ B_{\theta n}^c \end{bmatrix} = \begin{bmatrix} F_o(\delta, \gamma) & G_o(\gamma, \delta) \\ G_o(\delta, \gamma) & F_o(\gamma, \delta) \end{bmatrix} \begin{bmatrix} A_{z,n}^b \\ A_{z,n}^c \end{bmatrix} - J_{fs} \begin{bmatrix} X_{fs} \\ Y_{fs} \end{bmatrix}, \quad (12)$$

where

$$\begin{aligned} J_{fs} &= \frac{\mu_o J_{zn}}{(np)^2 - 1}, \\ X_{fs} &= \gamma F_o(\delta, \gamma) + \delta G_o(\gamma, \delta) + 1, \\ Y_{fs} &= \gamma G_o(\delta, \gamma) + \delta F_o(\gamma, \delta) + 1. \end{aligned}$$

Note that J_{zn} refers to magnitude of current density distribution of n^{th} harmonic.

Using the described method, magnetic fields generated by the permanent magnet can be computed at a certain boundary, and can be superposed with the calculated magnetic field generated by the copper coils at the same boundary to evaluate the Maxwell Stress Tensor. Then the torque can be calculated as

$$Torque = \frac{D_{ag}}{4} \frac{\pi D_{ag} L_{stk}}{\Delta\theta \mu_o p} \langle B_n B_\theta \rangle, \quad (13)$$

where $\Delta\theta$ accounts for the spatial discretization and p refers to number of magnetic pole pairs. The model is tested at various pole counts and dimensions. Fig. 7 shows radial and tangential components of air-gap flux density of a 8-pole toothless machine and shows good agreement with FEA. This model can easily be applied to inner-rotor topology with boundaries and radii flipped.

B. Iron Loss

Numerous specific iron loss models have been proposed since Steinmetz' first formulation [15]–[17]. We found that the best model for specific iron loss allows for variable loss coefficients with frequency or induction, as presented in [18]. Using such method, specific iron loss in stator yoke with yoke flux density,

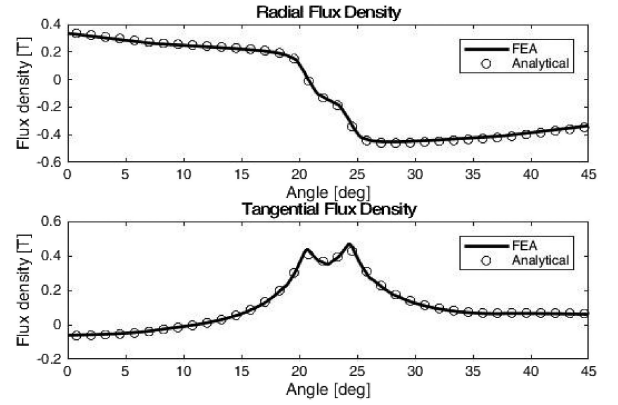


Fig. 7. Air-gap field comparison between FEA and analytical method of a 8-pole slotless motor with current density of $8 A/mm^2$ (peak). Radial and tangential components of total air-gap field (from permanent magnet and copper coils) are shown.

B_{yk} , varying at some frequency, f , can be realized as

$$P_{yk} = k_h f B_{yk}^2 + k_e f^2 B_{yk}^2 \quad (14)$$

where the hysteresis loss coefficient, k_h , and eddy current loss coefficient, k_e , are each characterized as a cubic polynomial:

$$\begin{aligned} k_h &= k_{h,0} + k_{h,1} B_{yk} + k_{h,2} B_{yk}^2 + k_{h,3} B_{yk}^3 \\ k_e &= k_{e,0} + k_{e,1} B_{yk} + k_{e,2} B_{yk}^2 + k_{e,3} B_{yk}^3 \end{aligned} \quad (15)$$

Then, heat flux (W/m^2) due to iron loss in the yoke can be expressed as,

$$q_{yk} = [k_h f B_{yk}^2 + k_e f^2 B_{yk}^2] \rho_{fe} d_{yk} \quad (16)$$

where ρ_{fe} and d_{yk} refer to volumetric mass density of yoke material and radial dimension of the yoke. Note that flux density in the yoke can be estimated as

$$B_{yk} = B_{ag} \frac{D_{ag}}{2d_{yk}p} \quad (17)$$

where B_{ag} and p refer to peak air-gap flux density and number of magnetic pole pairs.

C. Copper Loss

Copper losses can be separated into dc and ac losses and represented as heat flux. Heat flux due to dc conduction losses can be represented as

$$q_{dc} = [J_{cu}^2 / \sigma_{cu}] d_{cu} f f \quad (18)$$

where J_{cu} , σ_{cu} , d_{cu} , and $f f$ refer to copper current density, copper conductivity, radial dimension of copper coils, and copper fill factor. Heat flux due to ac losses, specifically proximity losses, can be represented as

$$q_{ac} = \frac{\omega_o^2 \bar{B}^2 D_{str}^2}{32 \rho_{cu}} d_{cu} f f \quad (19)$$

where ω_o , \bar{B}^2 , and D_{str} refer to frequency, spatial average of peak flux density squared, and copper strand diameter [19]. For the slot-less topology, \bar{B}^2 can be computed by mapping

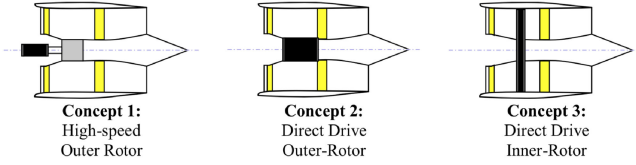


Fig. 8. Schematic of the STARC-ABL tail cone propulsor showing three possible locations for the motor.

the field within the winding region using the flux-potential transfer relations from Section III-A. Accuracy of the analytical model for copper losses have been verified via indirect balanced calorimetry [12].

D. Windage Loss

There are three major sources of mechanical losses for the discussed topology: air-gap windage, outer rotor windage, and cooling fan losses. Because the windage loss at the outer rotor surface is largely removed by the mass flow at the surface, airgap windage is considered as the only contributor to the airgap heat flux. Airgap windage losses have been estimated and experimentally verified as shown in [11]. Using the experimental measurements from the rotor test, heat flux from the air-gap windage loss at different speeds, N , and air-gap diameters, D_{ag} , can be estimated as

$$q_{wind} = q_{wind,base} \left[\frac{N}{N_{base}} \right]^{2.8} \left[\frac{D_{ag}}{D_{ag,base}} \right]^{3.5}, \quad (20)$$

where $q_{wind,base}$ refers to heat flux due to airgap windage measured for a motor with an air-gap diameter of $D_{ag,base}$ at speed of N_{base} .

IV. BLI PROPULSOR MOTOR OPTIMIZATION

While the baseline model was optimized at a power rating of 1 MW, STARC-ABL specification calls for a 2.6 MW power rating [8]. To optimize the air-core machine for the BLI propulsor, rated power of the motor is constrained at 2.6 MW at a speed of 3000 rpm. Upon examining the geometry of the tailcone propulsor published in [8], three possible motor-fan integrations are realized:

- *Concept 1*: High-speed, outer rotor (fan driven via a gearbox)
- *Concept 2*: Direct-drive, outer rotor (motor located at the base of the fan blades)
- *Concept 3*: Direct-drive, inner-rotor (motor located at the tip of the fan blades, “rim-driven”)

These concepts are illustrated in Fig. 8. Concept 1, with an operating speed of 15,000 rpm, has the potential for highest specific power. However, with a need for a 5:1 gear, both efficiency and specific power may be reduced. The second concept is a direct drive motor, with operating speed of 3000 rpm. The last concept places the motor at the tip of the fan with an operating speed of 3000 rpm. Fig. 9 and Fig. 10 illustrate what concept 2 and concept 3 motors would look like when integrated to the fan.

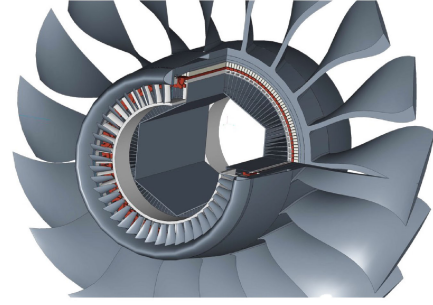


Fig. 9. CAD illustration of direct-drive, outer rotor motor and fan integration

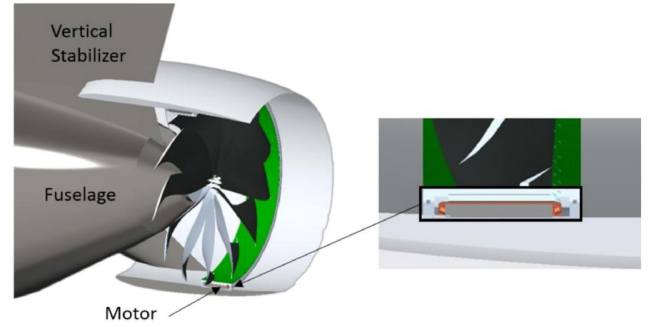


Fig. 10. CAD illustration of direct-drive, inner rotor rim-driven fan integration

A. Multi-Objective Optimization Scheme

For fair comparison of specific power and efficiency across different concepts, an evolutionary genetic algorithm toolbox for MATLAB, i.e., GOSET [20] was utilized to obtain a pareto optimal front for each concept. The optimization is performed within the design space of free variables,

$$V_{free} = [p \ d_{cu} \ d_{pm} \ L_{act}]^T \quad (21)$$

where p , d_{cu} , d_{pm} , and L_{act} refer to number of pole pairs, copper radial height, magnet radial height, and active length, respectively. Fixed variables are included to constrain the optimization problem as

$$V_{fixed} = [\omega_m \ q_{ag} \ P \ B_{yk} \ D_o]^T \quad (22)$$

where q_{ag} refers to total heat flux in the airgap such that $q_{ag} = q_{yk} + q_{dc} + q_{ac} + q_{wind}$. ω_m , P , B_{yk} , and D_o refer to mechanical angular speed, rated power, peak yoke flux density, and machine outer diameter, respectively. The heat flux in the airgap, denoted as q_{ag} , is fixed to that of the baseline design across different concepts and designs, as it is treated as a cooling specification. Experiences with the fan design from the baseline design point to the fact that $q_{ag} = 65 \text{ kW/m}^2$ is manageable with a 20 m/s airflow through the heat exchanger. While this assumption may not be completely true in other design concepts, it is useful in providing first order comparison between the concepts.

From the input, V_{free} , the algorithm generates candidate designs and outputs a pareto front that investigates tradeoff between total weight, W_{tot} , and efficiency, η , with fitness functions

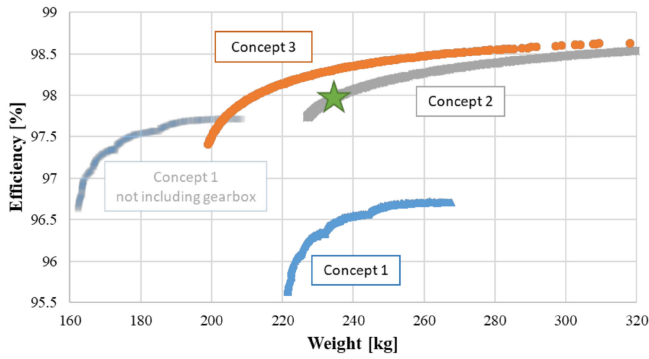


Fig. 11. Case study results showing pareto optimal front for three designs using genetic algorithm. The star symbol marks the final choice for BLI fan motor.

given by

$$f(V_{free}) = \left[\frac{1}{W_{tot}} \quad \frac{1}{\eta} \right]^T \quad (23)$$

To assess the total weight of a design, a detailed CAD model is used. With information from the baseline design, radial dimensions of structural components such as titanium, shell and carbon fiber retaining ring can be scaled for various rotor tip-speeds. The effect of stack length on end plate thickness is also included to account for static deflection (thickness of end plate $\propto 1/L_{stack}$) [21]. In addition to materials, fixed Litz wire strand diameter, fill factor, yoke lamination thickness is also enforced. Note that the strand diameter is chosen to accommodate the skin depth at maximum frequency used in the study.

B. Optimization Results and Concept Comparison

Fig. 11 shows the results from the optimization study, as generated with 1000 individual, 30 generation optimization run per design. For the concept 1, gearbox loss of 1% is assumed and weight of the gearbox estimated using empirical correlations from a survey of numerous gearboxes used in aircraft applications [22].

Upon comparison of the results, the benefit of 15000 rpm, outer rotor motor is once again highlighted. With not only high rotational speed, but also high tip speed, motor designed for concept 1 displays the lowest weight among the three motors. However, when the effect of gearbox is added, the high-efficiency, low-weight characteristics are quickly lost. The outer-rotor motor (concept 2) in the plot shows potential for high efficiency, at the cost of weight. The observed heavy weight characteristic is in agreement with the fact that low rotor tip speed causes reduction in specific power. With a speed-constraint of 3000 rpm and outer diameter constraint of 23 inches, tip speed of the motor is constrained to 1/4 to that of concept 1 and concept 3 motors. The rim-driven fan design, however, has high tip speeds even at low rpm due to a significant outer diameter. The benefit of high tip speed is clear, while the high-frequency causes slightly lower efficiency. Furthermore, because the rotor is no longer on the outside of the motor, cantilevered design and its associated auxiliary weight can be eliminated. With an outer stator, the need for aluminum heat exchanger can also be eliminated since

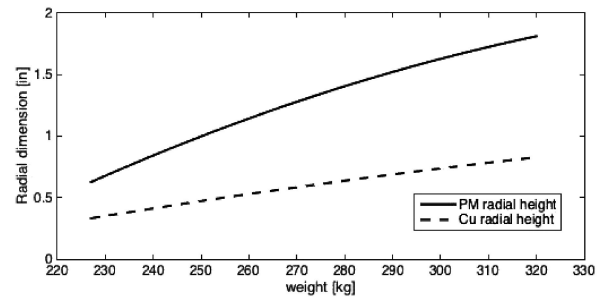


Fig. 12. PM radial height and coil radial height for different designs for concept 2.

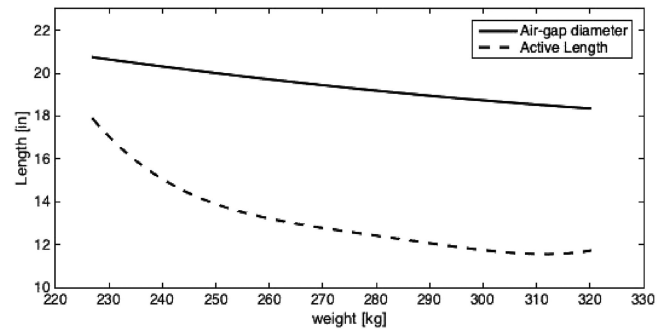


Fig. 13. Air-gap diameter and stack length for different designs for concept 2.

the heat due to copper and iron losses can be directly extracted from the outer diameter of the machine. While this rim-driven fan topology seems optimal at a glance, having electromagnetic interaction at such a large diameter comes with significant mechanical risks and difficulty identifying appropriately rated bearings, and thus may not be a feasible concept.

A common parameter that drives the weight-efficiency trade-off for the three concepts is found to be pole-count (or rather, frequency). For example, an examination of the pareto front for concept 2 shows that the design with lowest efficiency and weight has 40 poles (1000 Hz), whereas the design with highest efficiency and weight has 14 poles (350 Hz). The 40 pole design is characterized by a very thin radial build at the expense of high ac losses, where the opposite is true for the 14 pole design. This is illustrated in Fig. 12, where both magnet radial height and copper radial height is observed to reduce due to high pole count designs toward the left of the curve.

Figures 13 and 14 provide more insight to the trade-off between weight and efficiency of the most favorable concept - concept 2. Because of the reduced radial dimensions for the magnet and the constrained outer dimension, airgap diameter is allowed to increase, as seen in Fig. 13. It is also interesting to note that these low-weight, low-efficiency designs demonstrate longer active length than the designs on the far right. This indicates that the effect of higher-pole, higher-frequency designs on reduction in weight is greater than the effect of longer active length. Fig. 14 shows a trend in reduced electrical loading and magnetic loading for low-efficiency, low-weight designs to accommodate higher losses.

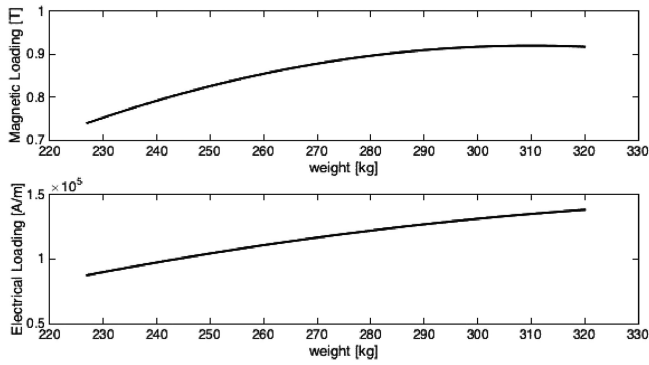


Fig. 14. Electrical and magnetic loading for different designs for concept 2.

TABLE II
KEY METRICS AND DIMENSIONS FOR THE SELECTED MOTOR

Rated Power	2.6	MW
Rated Efficiency	98	%
Nominal Speed	3000	rpm
Cooling, Forced air	20	m/s
Tip Speed	93.76	m/s
Outer Diameter	23.5	in.
Number of Poles	32	-
PM Radial Thickness	0.84	in.
Air-gap Diameter	20.3	in.
Coil Radial Thickness	0.40	in.
Stator Yoke Radial Thickness	0.36	in.
Physical Airgap	0.094	in.
Stack Length	15.3	in.
Specific Power	11	kW/kg
Total Weight	230	kg

V. SELECTED DESIGN

With various considerations discussed in the previous section, final concept and design is chosen and marked by the star symbol in Fig. 11. While the weight of the machine is critical for aircrafts, additional 2 points of efficiency over the assumed 96% metric used in the STARC-ABL feasibility study in [8] is expected to be valuable in propulsion system context. Key metrics and dimensions for the final design can be found in Table II. Motor voltage is determined to be 650 V (rms, line-line). Modular inverters should be used to drive the motor to accommodate the appropriate current ratings.

Electromagnetic performance and power rating of 2.6 MW is verified using FEA, where the model shown in Fig. 15 highlights the thin radial build of the topology. Loss breakdown of the machine is shown in Fig. 16. With tip speed that's only a third of the baseline 1 MW design, the percentage of windage losses is found to be much lower (compared to 70% of the losses being windage in the baseline motor). As a result, a bigger percentage of airgap heat flux can be allocated to copper losses, allowing for a larger electrical loading (2.3 times larger), and thus maintaining a >10 kW/kg of specific power. The hotspot temperature for this design has been analysed using thermal FEA as shown in Fig 17. A periodic model with one coil segment was used to reduce the computational expense while capturing the most important heat transfer considerations. A heat generation of 225 W was applied to the copper coils. This value corresponds

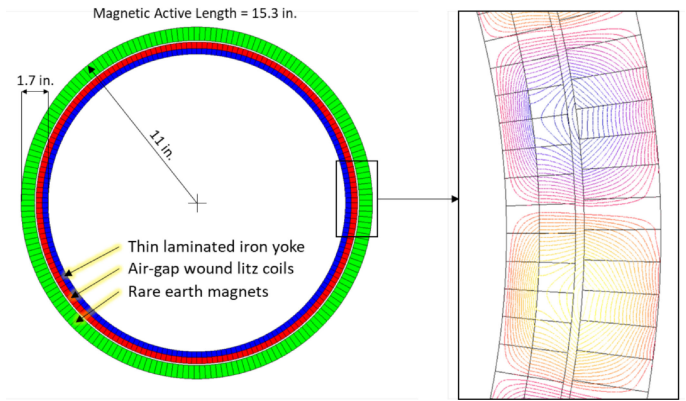


Fig. 15. Electromagnetic finite element model and resulting magnetic field lines.

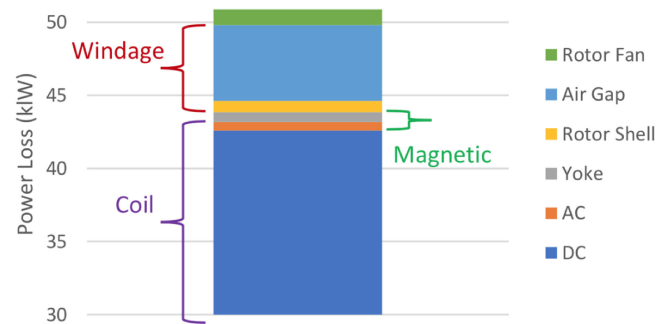


Fig. 16. Loss breakdown of the selected design.

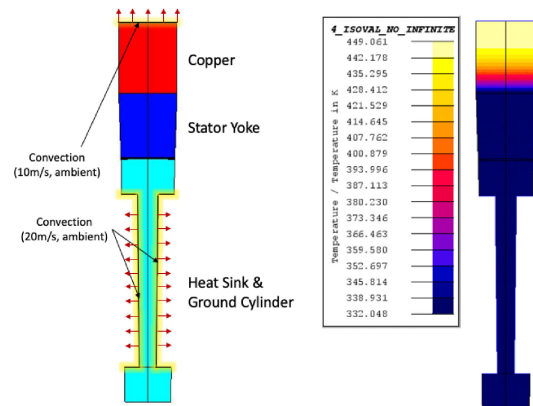


Fig. 17. Thermal finite element model and resulting heatmap.

to the total expected copper losses divided by the number of coil segments. Iron loss and windage loss at the airgap has also been included in the study. Across the heat sink, a convection boundary condition was applied with an air flow of 20 m/s at an ambient temperature of 23 °C. More moderate cooling is assumed in the airgap with an air flow of 10 m/s [13]. These assumptions are analogous to the studies performed for the baseline design [13]. The results show that the copper coils operate at an average temperature of about 150 °C, with a hotspot temperature of 176 °C. This 2-dimensional analysis shows that

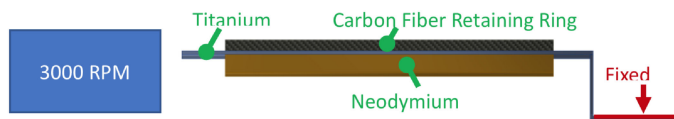


Fig. 18. Mechanical boundary conditions for rotor finite element analysis.

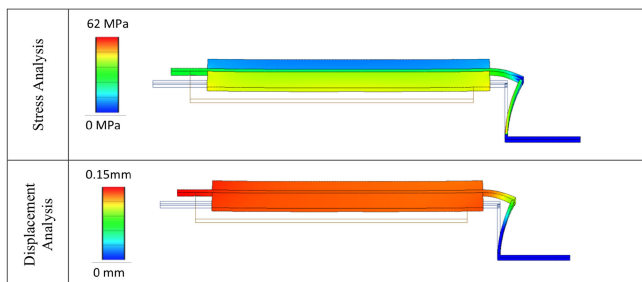


Fig. 19. Results of retaining ring structural analysis.

the hotspot temperature is within the temperature rating of Class H insulation intended for the coils. However, a more rigorous investigation considering the effects of atmospheric conditions at altitude and 3-d effects must be performed. For example, while the temperature at cruise altitude is around -56.5°C , and can greatly help management of thermal losses, proper design into fans have to be considered as the atmospheric pressure drops by a factor of five (compared to sea level).

Mechanical analysis on the retaining ring is also performed to ensure integrity of the rotor structure. This is important to ensure proper contacts with the bearings, which do not provide any support in tension. A static FEA was performed using Autodesk Inventor on a periodic section of the rotor. Boundary conditions and material properties were prescribed as shown in Fig. 18. The right end of the rotor is assumed not to expand due to added material from the fan and is set as a fixed boundary condition. The left end of the motor is open to expand. This direct drive motor is assumed to spin with a fan speed of 3000 RPM to generate radial body forces pointing away from the center of the motor. Note that the mechanical simulations were performed using retaining ring material properties at room temperature. The effects of heat flux from the coils on the carbon fiber retaining ring and titanium are neglected in this analysis, because of convective cooling in the airgap. The heat flux due to windage at the rotor outer diameter is found to be small (as seen in Fig. 16) and thus also excluded for this analysis. The results of the finite element analysis are presented in Fig 19. The maximum stress experienced in both the rotor shell and retaining ring are well below the endurance life of carbon fiber and titanium, where endurance life is taken as half of the ultimate strength. The maximum displacement of the rotor is near 0.15 mm validating the ability of retaining ring to keep the rotor in contact with the bearings.

CAD rendering of the chosen direct-drive 2.6 MW BLI fan motor is shown in Fig. 20. Note that the fan design shown in the figure is not optimized to force air through the heat exchangers, and only serves graphic purposes. Next iteration

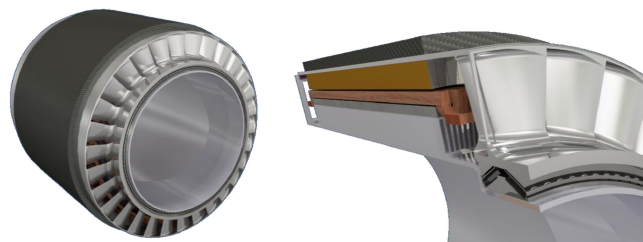


Fig. 20. CAD rendering of concept 2 motor selected from design optimization results. Fan and bearing design shown in the rendering is not representative of the final design.

of design optimization will be performed in conjunction with a propulsor fan design, where the effects of fan dynamics will be taken into account. Furthermore, because of substantial axial load associated with propulsors, proper bearing choices will need to be made.

VI. CONCLUSION

The design of a motor for a tail-cone BLI fan, based on a 1MW prototype, has been investigated. An analytical model utilizing electromagnetic transfer relation, validated with finite element analysis, is presented. In addition, major losses mechanisms have been characterized and incorporated within a genetic algorithm based optimization scheme. Efficiency-weight tradeoff is observed for all three proposed concepts to show that the direct-drive, outer rotor motor and fan integration is most attractive. A design on the pareto curve that exhibits a good balance between efficiency and weight is chosen, and initial analyses have been performed. The final design is a 2.6 MW, 3000 rpm motor with 98% efficiency at a specific power of 11 kW/kg.

REFERENCES

- [1] M. D. Hathaway, R. Del Rosario, and N. Madavan, "Nasa fixed wing project propulsion research and technology development activities to reduce specific energy consumption," in *Proc. 49th AIAA/ASME/SAE/ASEE Joint Propulsion Conf.*, 2013, pp. 3605–3625.
- [2] X. Zhang, C. L. Bowman, T. C. O'Connell, and K. S. Haran, "Large electric machines for aircraft electric propulsion," *IET Electric Power Appl.*, vol. 12, no. 6, pp. 767–779, 2018.
- [3] A. M. EL-Refaie *et al.*, "Advanced high-power-density interior permanent magnet motor for traction applications," *IEEE Trans. Industry Appl.*, vol. 50, no. 5, pp. 3235–3248, Sep. 2014.
- [4] D. Gerada, A. Mebarki, N. L. Brown, C. Gerada, A. Cavagnino, and A. Boglietti, "High-speed electrical machines: Technologies, trends, and developments," *IEEE Trans. Ind. Electron.*, vol. 61, no. 6, pp. 2946–2959, Jun. 2014.
- [5] P. Arumugam *et al.*, "High-speed solid rotor permanent magnet machines: Concept and design," *IEEE Trans. Transp. Electrification*, vol. 2, no. 3, pp. 391–400, Sep. 2016.
- [6] A. Yoon, X. Yi, J. Martin, Y. Chen, and K. Haran, "A high-speed, high-frequency, air-core pm machine for aircraft application," in *Proc. IEEE Power Energy Conf. Illinois*, Feb. 2016, pp. 1–4.
- [7] A. Yoon and K. Haran, "Scaling study of high frequency machine for electric aircraft propulsion," in *Proc. IEEE Energy Convers. Congr. Expo.*, Sep. 2018, pp. 4439–4444.
- [8] J. Welstead *et al.*, "Overview of the NASA STARC-ABL (Ref. B) advanced concept," in *Proc. One Boeing NASA Electric Aircraft Workshop*, 2017, pp. 1–14.

- [9] J. Welstead and J. L. Felder, "Conceptual design of a single-aisle turboelectric commercial transport with fuselage boundary layer ingestion." [Online]. Available: <https://arc.aiaa.org/doi/abs/10.2514/6.2016-1027>
- [10] C. B. Barth *et al.*, "Design and control of a GaN-based, 13-level, flying capacitor multilevel inverter," in *Proc. IEEE 17th Workshop Control Model. Power Electron.*, Jun. 2016, pp. 1–6.
- [11] R. Sanchez *et al.*, "Mechanical validation of a high power density external cantilevered rotor," *IEEE Trans. Industry Appl.*, vol. 54, no. 4, pp. 3208–3216, Jul. 2018.
- [12] J. Martin, A. Yoon, A. Jin, and K. S. Haran, "High-frequency litz air-gap windings for high-power density electrical machines," *Electric Power Compon. Syst.*, vol. 45, no. 7, pp. 798–805, 2017. [Online]. Available: <https://doi.org/10.1080/15325008.2017.1310951>
- [13] X. Yi, R. Sanchez, K. Haran, J. Veres, A. T. Perry, and P. J. Ansell, "Self-pumped air-cooling design for a high-speed high-specific-power motor," in *Proc. IEEE Transp. Electrification Conf. Expo.*, Jun. 2018, pp. 274–279.
- [14] J. R. Melcher, *Continuum Electromechanics*. Cambridge, MA, USA: MIT Press, 1981.
- [15] C. P. Steinmetz, "On the law of hysteresis," *Proc. IEEE*, vol. 72, no. 2, pp. 197–221, Feb. 1984.
- [16] J. Hendershot and T. Miller, *Design of Brushless Permanent-Magnet Machines*. Venice, FL, USA: Motor Design Books, 2010.
- [17] T. J. E. Miller and M. I. McGilp, *PC-BDC 6.5 for Windows-Software*, Glasgow, U.K.: SPEED Laboratory Univ., 2004.
- [18] D. M. Ionel, M. Popescu, S. J. Dellinger, T. J. E. Miller, R. J. Heideman, and M. I. McGilp, "On the variation with flux and frequency of the core loss coefficients in electrical machines," *IEEE Trans. Industry Appl.*, vol. 42, no. 3, pp. 658–667, May 2006.
- [19] C. R. Sullivan, "Computationally efficient winding loss calculation with multiple windings, arbitrary waveforms, and two-dimensional or three-dimensional field geometry," *IEEE Trans. Power Electron.*, vol. 16, no. 1, pp. 142–150, Jan. 2001.
- [20] S. Sudhoff, *Optimization-Based Design*. Piscataway, NJ, USA: IEEE Press, 2014.
- [21] Y. Chen, R. Sanchez, A. Yoon, and K. S. Haran, "Mechanical design considerations of an ironless, high-specific-power electric machine," *IEEE Trans. Transp. Electrification*, vol. 3, no. 4, pp. 855–863, Dec. 2017.
- [22] T. Krantz, "Gearbox weight estimation," NASA Glenn Res. Center, Cleveland, OH, USA, Tech. Rep., 2002.



Jianqiao Xiao received the B.S. degree in electrical and computer engineering from the University of Illinois at Urbana Champaign, Urbana, IL, USA, in 2019, where he is currently working toward the M.S. degree in electrical engineering in the area of electric machines.

His research interests include electro-mechanical design of electric machines.



Danny Lohan received the B.S. degree in general engineering from the University of Illinois at Urbana Champaign, Urbana, IL, USA, in 2014, where he is currently pursuing the Ph.D. degree in systems engineering. His research interests include the parameterization and automation of engineering design problems. He works on design optimization at Hinetics LLC, Urbana, IL, USA.



Faraz Arastu is currently working toward the Ph.D. degree in materials engineering with the University of Illinois at Urbana Champaign, Urbana, IL, USA. He has experience in both microelectronics and composites industries, with a focus on mechanical design and manufacturing. He works on system integration at Hinetics.



Andy Yoon (S'13) received the B.S. and M.S. degrees in electrical and computer engineering from the University of Illinois at Urbana Champaign, Urbana, IL, USA, in 2013 and 2016, respectively, where he is currently working toward the Ph.D. degree in optimization of electric machines for aviation propulsion applications. His research interests include high speed, high-frequency electromechanical devices for weight and volume sensitive applications.



Kiruba Haran (M'95–F'14) received the Ph.D. degree in electric power engineering from Rensselaer Polytechnic Institute, Troy, NY, USA, in 2000. He was with GE Global Research Center in Niskayuna, NY, USA, for 13 years, first as an Engineer and then Manager of the Electrical Machines Laboratory. In 2014, he moved to the University of Illinois at Urbana-Champaign, to join the Grainger Center for Electric Machinery and Electromechanics and the Department of Electrical and Computer Engineering.